Semmling, M., Wickert, J., Schön, S., Stosius, R., Markgraf, M., Gerber, T., Ge, M., Beyerle, G. (2013): A zeppelin experiment to study airborne altimetry using specular Global Navigation Satellite System reflections. - *Radio Science*,*48*, 4, 427-440

DOI: 10.1002/rds.20049

RADIO SCIENCE, VOL. 48, 427–440, doi:10.1002/rds.20049, 2013

# A zeppelin experiment to study airborne altimetry using specular Global Navigation Satellite System reflections

A. M. Semmling,[1] J. Wickert,[1] S. Schön,[2] R. Stosius,[3] M. Markgraf,[4] T. Gerber,[1] M. Ge,[1] and G. Beyerle[1]

Received 8 April 2013; revised 20 June 2013; accepted 2 July 2013; published 15 August 2013.

[1] This paper describes an altimetric method based on data recorded during experimental zeppelin flights over Lake Constance. Interferometric observations for this method are obtained using a Master-Slave receiver configuration. These observations contain the relative phasing of direct and reflected signals and are used for altimetry. Separated antennas are attached to the receiver to record direct and reflected signals at slant elevation angles. Filtering is required to remove direct contributions in this slant geometry. Filtered observations are corrected using an altimetric model, and thus Doppler residuals are retrieved. This correction reduces the width of the spectral reflection peak from 3 mHz to less than 10 mHz. Doppler residuals are sensitive to surface height. Lake level is estimated inversely for the residuals at different trial heights. A case study of reflection events is presented. Lake level is estimated using data from antennas with right-handed and left-handed circular polarization. Reference level is determined from tide gauge data for stations around the lake. Mean deviation of estimates from reference level is 50 cm. Doppler shifts of different model corrections are compared. The altimetric correction is the most important, with mean Doppler shifts between 316 and 560 mHz. Mean Doppler shifts are much smaller for baseline correction (less than 0.2 mHz) and water-vapor correction (0.1–1.0 mHz). In addition, the geoid undulation effect (up to 25 cm amplitude) is predicted with mean Doppler shifts between 0.1 and 0.9 mHz. Precision of Doppler residuals (0.5–0.6 mHz) is insufficient to resolve the geoid undulation effect. The resolution from phase residuals is better. The effect of geoid undulation, however, is not dominant in phase residuals.

**Citation:** Semmling, A. M., J. Wickert, S. Schön, R. Stosius, M. Markgraf, T. Gerber, M. Ge, and G. Beyerle (2013), A zeppelin experiment to study airborne altimetry using specular Global Navigation Satellite System reflections, *Radio Sci.*, *48*, 427–440, doi:10.1002/rds.20049.

## 1. Introduction

[2] Remote sensing techniques are important for global investigations of climate change and disaster monitoring. Spaceborne radar altimeters are powerful tools, particularly for ocean observations indicating climate change. Long-term variations of mean sea level on a global scale have been resolved using radar altimeters [*Nerem et al.*, 2010]. They are also crucial in monitoring the variability of large scale ocean phenomena such as El Niño, monsoons, or the North Atlantic oscillation [*Xu et al.*, 2011]. A major part of the World's ocean variability, however, arise from large oceanic eddies [*Chelton et al.*, 2001] whose observation requires a better temporal and spatial resolution of the ocean surface than is provided by a single radar altimeter.

[3] Resolution is even more challenging if early detection of a tsunami is investigated. The December 2004 Indian Ocean tsunami was overflown by a radar altimeter when 1 h, 53 min had already elapsed since the initial earthquake [*Ablain et al.*, 2006]. Radar altimeter observations are limited to ocean coverage and repetition time of a single surface track. A significantly higher coverage of tracks is anticipated for an altimeter using GNSS (Global Navigation Satellite System) reflections. The large number of synchronized GNNS transmitters yields various reflection tracks of GNSS signals observed simultaneously by a single spaceborne receiver.

[4] Improvements in ocean coverage and probability of tsunami detection with GNSS reflectometry (GNSS-R) have been shown in a simulation study [*Stosius et al.*, 2010].

[1]Department of Geodesy and Remote Sensing, Deutsches GeoForschungsZentrum, Potsdam, Germany.
[2]Institut für Erdmessung, Leibniz Universität, Hannover, Germany.
[3]Enviscope GmbH, Frankfurt, Germany.
[4]Space Flight Technology, Deutsches Zentrum für Luft- und Raumfahrt, Wessling, Germany.

Corresponding author: A. M. Semmling, GeoForschungsZentrum Potsdam (GFZ), Department 1, Geodesy and Remote Sensing, Telegrafenberg, 14473 Potsdam, Germany. (maxsem@gfz-potsdam.de)


0048-6604/13/10.1002/rds.20049

Various experiments on GNSS-R have been conducted during the last two decades, prompted especially by the PARIS (Passive Reflectometry and Interferometry System) concept [*Martín-Neira*, 1993]. An overview on methods and applications of GNSS-R can be found in *Cardellach et al.* [2011].

[5] For altimetry, the specular part of the reflection is considered. This means those rays with equal angles of incidence and reflection at the so-called specular surface point. Airborne experiments on ocean altimetry have been conducted [*Lowe et al.*, 2002; *Ruffini et al.*, 2004; *Rius et al.*, 2012] (inter alia). Corresponding methods use code delay maps to determine the height of the specular point (specular height). Inversion of wind-induced surface roughness has been examined theoretically [*Zavorotny and Voronovich*, 2000] and experimentally [*Garrison and Katzberg*, 2000; *Gleason et al.*, 2005] (inter alia). Code delay and Doppler information are mapped to study diffuse ocean scattering which depends on wind velocity.

[6] Sampling of Delay Maps for altimetry and Delay-Doppler Maps for wind inversion demand considerable GNSS receiver resources. Appropriate receivers perform multiple samplings simultaneously [*Nogués-Correig et al.*, 2007]. The GORS (GNSS Occultation Reflectometry Scatterometry) receiver used in this study had already been set up for ground-based altimetry [*Semmling et al.*, 2011]. It provides interferometric observations based on two samplings (Master-Slave configuration) that demand less resources (comparable to common geodetic receivers). An upgraded GORS receiver for airborne altimetry is described in this paper.

[7] Provided that interferometric phase observations are continuous (coherent reflection), a better altimetric precision is anticipated compared to Delay Maps. Phase retrievals have been used for centimeter-precision lake altimetry in ground-based setups [*Treuhaft et al.*, 2001]. For typical ocean roughness conditions, however, the required continuity of observations is lost. Doppler residuals have been used instead for decimeter-precision ocean altimetry [*Semmling et al.*, 2012].

[8] Doppler residuals related to GNSS reflections have already been considered within spaceborne Radio Occultation setups [*Beyerle et al.*, 2002]. Such reflections are located over the ocean and in the polar regions. There, surface layers contain liquid water that is highly polarisable by L band radio waves giving high reflectivity. Grazing elevation angles encountered in occultation setups reduce the roughness effect on the interferometric phase. The *Fraunhofer Criterion* describes the fundamental relation of surface roughness, signal wavelength, and elevation angle [*Beckmann and Spizzichino*, 1987].

[9] The reduced roughness effect at grazing angles increases the number of useful reflections. However, the sensitivity of reflections to the surface height is reduced at these angles. A height difference of 1 m causes a significant phase shift of about 10 cycles at an elevation of 90°. The corresponding shift of less than 0.2 cycles at 1° is hardly detectable considering that phase noise often exceeds this value. Despite this low sensitivity at grazing angles, decimeter-precision ice-sheet altimetry has been reported for reflection data in Radio Occultation events [*Cardellach et al.*, 2004].

[10] This paper describes airborne altimetry with the GORS receiver using interferometric carrier observations. The paper consists of six sections. Section 1 provided an introduction to airborne GNSS-R altimetry. Section 2 summarizes the flights conducted over Lake Constance. Interferometric observations of direct and reflected signals and two example events are described in section 3. The altimetric method based on phase path models and filtered observations are addressed in section 4. Results for different reflection events are presented in section 5 including a discussion of modeled effects and the additional effect of surface undulation. Section 6 summarizes this altimetric study.

## 2. Flights Over Lake Constance

[11] Flights with the zeppelin airship were conducted over Lake Constance, situated between Austria, Germany, and Switzerland. A map in Figure 1 shows the lake and all important locations.

[12] The lake extends over a length of 63.5 km from *Ludwigshafen* {6} to *Bregenz* {1}. It is 12.5 km wide between *Friedrichshafen* {3} and *Romanshorn* {4}. The maximum depth at the center between {3} and {4}, is ≈ 250 m. Geoid undulations of more than 0.5 m amplitude are predicted by the Combined German QuasiGeoid model (GCG-05) [*Liebsch et al.*, 2006] affecting the lake surface.

[13] Flights considered in this paper were conducted on 12 October 2010 between 5 h, 38 min and 16 h, 40 min GPS time. A light breeze from the east was reported for this day with max. wind speed of 5.9 m/s at lake level. The two flights consisted of six legs along the lake (Figure 1). They covered a total distance of 525 km in 9 h, 20 min that corresponds to an average ground speed of 56 km/h. The maximum ground speed was 82 km/h. A cruising altitude between 300 and 800m above lake level was requested. A tolerance range was needed to avoid clouds in order to meet visual flight rules. A code-based position with a height precision better than 10 m was determined by the GORS receiver in real-time to track reflection's code delay, cf. equation (4) below. An aircraft trajectory with 5 Hz sampling and a height precision of about 10 cm was estimated in postprocessing using regional augmentation [*Ge et al.*, 2012]. Along with the precise trajectory, the airship's attitude (roll, pitch, and yaw angles) was recorded with 10 Hz sampling using an inertial navigation system.

## 3. Interferometric Observation

[14] Geodetic GNSS receivers have dedicated algorithms to track the carrier phase of the incoming signal. If the incoming signal has overlapping direct and reflected contributions, the receiver provides interferometric observations. This means even after tracking observations oscillate due to the different phasing of contributions. A typical example is carrier phase multipath, where oscillations are observed in the sampled signal amplitude and in the derived SNR (signal-to-noise ratio) [*Bilich et al.*, 2008]. These multipath oscillations are restricted to a sampling of overlapping direct and reflected waveforms (code domain correlations) [*Borre et al.*, 2007]. When the reflection delay exceeds a limit of 1.5 chips, waveforms are separated and only a single

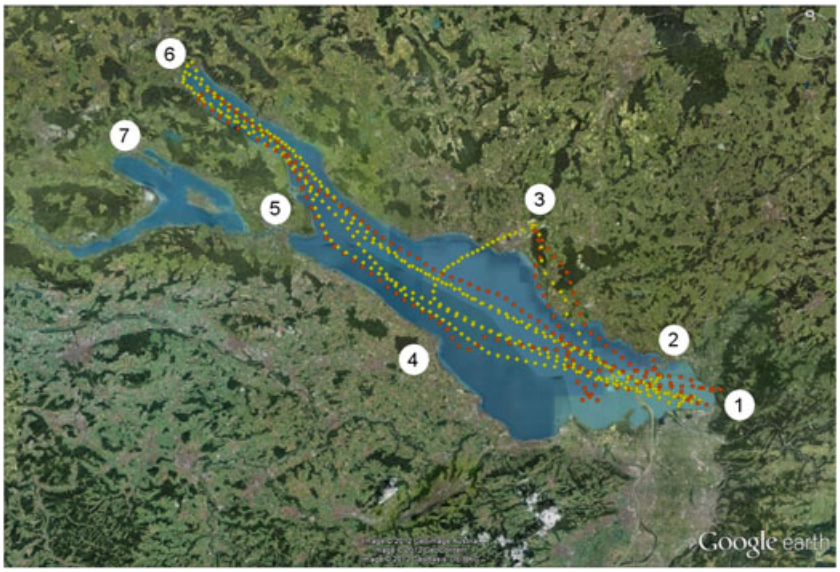


**Figure 1.** Lake Constance and surrounding locations ordered from east to west: {1} Bregenz, {2} Lindau, {3} Friedrichshafen, {4} Romanshorn, {5} Constance, {6} Ludwigshafen, and {7} Radolfzell. Two flight tracks are shown: red flight track (5 h, 38 min–8 h, 52 min GPS time) with waypoints {3}-{1}-{6}-{1}-{3} and yellow flight track (10 h, 34 min–16 h, 40 min GPS time) with waypoints {3}-{1}-{6}-{1}-{6}-{1}-{3}.

contribution is sampled. In this case a geodetic receiver does not provide interferometric observation.

[15] The GORS receiver is dedicated to remote sensing applications. It provides interferometric observations at tunable delays because of two different samplings in the code domain: the so-called Master sampling for the direct waveform and the so-called Slave sampling for the reflected waveform. A GORS prototype with a single antenna front-end had been used previously for ground-based ocean altimetry [*Semmling et al.*, 2011]. An enhanced GORS receiver is used in the zeppelin experiment based on a JAVAD geodetic receiver platform with a Quattro-G3D board. Master and Slave samplings are assigned to different front-ends. Firmware has been modified accordingly. An up-looking RHCP (right-hand circularly polarized) antenna is connected to the Master front-end. Two down-looking antennas, an RHCP one and an LHCP (left-hand circularly polarized) one, are connected to the Slave front-ends. The implementation of Master-Slave sampling in the zeppelin experiment is introduced in the first part of this section. This is followed by a discussion of interferometric observations for two different events.

### 3.1. Master-Slave Sampling

[16] For the zeppelin experiment, separated Master and Slave antennas were used. They were mounted with a short baseline at the rear of the airship (Figure 2).

[17] This layout is designed to separate direct and reflected signals. The Master antenna points upward to maximize direct signals' contribution from above and to optimally suppress reflections. Both Slave antennas point downwards with a tilt angle of 60° to receive one-sided reflected signals from starboard. This tilt helps to increase Slave antennas' gain of reflected signals at slant elevations. However, due to the slant geometry, the Slave antenna also sees direct contributions.

[18] The receiver provides Master and Slave samples at 200 Hz. Earlier data levels inside the receiver are not accessible, therefore simulations are presented here to illustrate sampling under ideal conditions when direct and reflected signals can be received separately by Master and Slave antennas respectively.

[19] Master sampling applies a tracking algorithm to adjust code delay, Doppler frequency, and carrier phase of a signal replica to the incoming signal at the Master antenna (Master replica). Slave sampling generates a copy of the Master replica corrected by open-loop tracking (Slave replica). This tracking adds a code delay $\Delta\tau$ to account for the relative delay of reflection with respect to the direct signal. The $\Delta\tau$-correction is discussed later for the two example events. A Doppler shift correction of the Slave replica is not necessary. The Doppler difference between direct and reflected signals can be resolved interferometrically by 200 Hz sampling which is much higher than the relative shift between both signals in the zeppelin experiment.

[20] In phase ($I$) and Quadrature ($Q$), components are recorded for carrier wipeoff and code wipeoff, cf. literature [*Misra and Enge*, 2001]. Simulations in Figure 3 illustrate the difference in carrier wipeoff for Master and Slave sampling.

[21] Slave sampling combines a replica model of the direct with the observed reflected signal. Under these ideal conditions Slave samples contain only one signal contribution, the specularly reflected one. Under general conditions the sum of direct and reflected contributions must be considered as shown in a phase diagram (Figure 4).

[22] This study disregards reflected contribution affecting Master sampling (multipath effect while tracking the direct

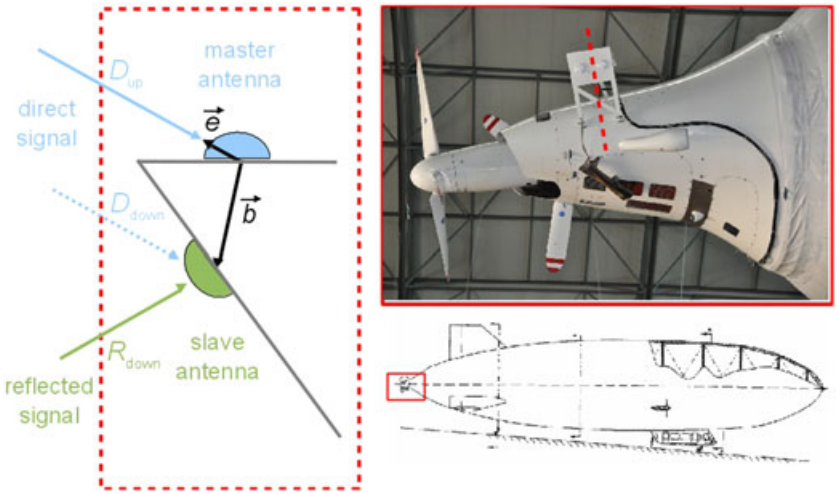


**Figure 2.** Location of antennas mounted on the zeppelin airship. The picture on the right shows the antenna mount at the rear. The scheme on the left shows signal contributions that have to be considered: Direct contributions received by Master antenna and direct and reflected contributions received by Slave antennas.

signal). The diagram contains tracked Master observations $\gamma_{mst}$ and interferometric Slave observations $\gamma_{slv}$ in phasor representation. The phasor $\gamma$ combines components $I$, $Q$

$$\begin{aligned} \gamma &= I + \mathrm{i}Q \\ &= |\gamma| \mathrm{e}^{-\mathrm{i}\phi}, \end{aligned} \tag{1}$$

and yields an amplitude $|\gamma|$ and a phase argument $\phi$. Master and Slave observations $\gamma_{mst}$ and $\gamma_{slv}$ are thus defined. The diagram also shows phasor models ($\gamma_{drc}$ and $\gamma_{rfl}$) to identify direct and reflected contributions in Slave observations

$$\begin{aligned} \gamma_{slv} &= \gamma_{drc} + \gamma_{rfl} \\ &= |\gamma_{drc}| \mathrm{e}^{-\mathrm{i}\phi_1} + |\gamma_{rfl}| \mathrm{e}^{-\mathrm{i}[\phi_1+\phi_2]}. \end{aligned} \tag{2}$$

[23] Two phase angles $\phi_1$ and $\phi_2$ are considered. These wrapped phase angles in units of radian are related to the optical phase path in units of cycles $\varphi = \phi/2\pi + n$ with $n$ being the integer ambiguity (number of completed cycles). Based on the scheme of antennas in Figure 2, the phase paths are modeled as follows:

$$\begin{aligned} \varphi_1 &= \frac{1}{\lambda}[D_{slv} - D_{mst}], \\ \varphi_2 &= \frac{1}{\lambda}[R_{slv} - D_{slv}], \\ \varphi_1 + \varphi_2 &= \frac{1}{\lambda}[R_{slv} - D_{mst}], \end{aligned} \tag{3}$$

where $\lambda$ is the L band wavelength, $R_{slv}$ is the reflected path (in meter) to Slave antenna and $D_{slv}$, $D_{mst}$ are the direct paths (in meter) to Master and Slave antennas, respectively.

[24] Before a detailed description of models $\varphi_1$ and $\varphi_2$ is provided in the altimetric method, two example events for satellites identified by pseudo random noise (PRN) number are considered to illustrate the interferometric observations. The first event starts shortly before take-off when the zeppelin is still on ground. The second is recorded when the zeppelin is airborne.

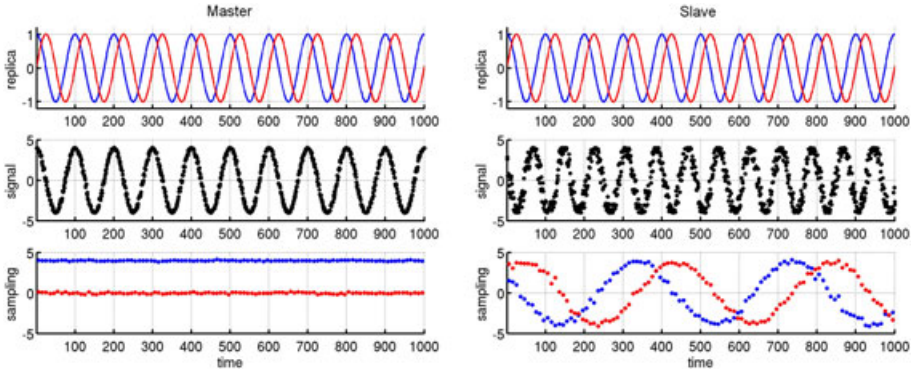


**Figure 3.** Simulations of carrier wipeoff for (left) Master sampling and (right) Slave sampling. Identical carrier replica are generated for Master and Slave with $I$ and $Q$ components in blue and red, respectively (top panels). Simulated front-end signals differ in frequency and phase (middle panels). Noise has been added to the signals in the simulation. An obvious difference occurs in the samplings (bottom panels). The Master shows constant components with $I$ being at max amplitude and $Q$ being almost zero. The Slave shows components $I$ and $Q$ oscillating with the frequency difference between signal and replica.

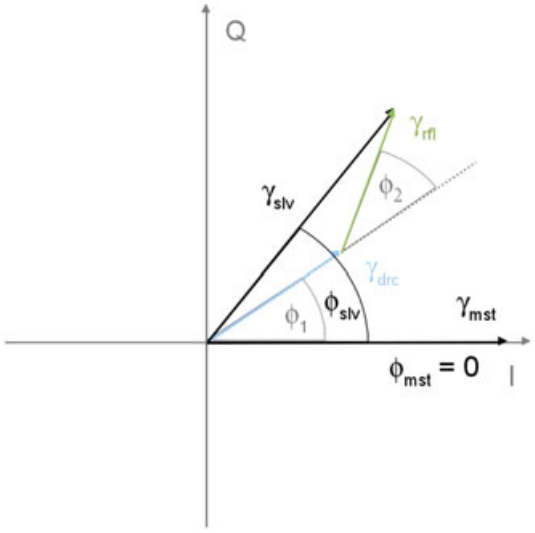


**Figure 4.** Phase diagram for Master and Slave observations. The phase of the direct signal is properly tracked, the residual Master phase $\phi_{mst}$ is zero. Contributions $\gamma_{drc}$, $\gamma_{rfl}$ sum up to the interferometric Slave phasor.

### 3.2. On-ground Reflection Event

[25] Reflection event PRN 12—12 October 2010 5 h, 28 min was recorded shortly before take-off over the grass-covered airfield at Friedrichshafen {3}. Master samples confirm a proper phase tracking of the direct signal, with maximum $I$ component and vanishing $Q$ component (Figure 5, top panel).

[26] For current on-ground events, there is an almost complete overlap of direct and reflected waveforms. The relative code delay $\Delta\tau$ is smaller than sampling resolution of 0.1 chip (C/A code) and can be disregarded. Slave sampling has the same offset in code and Doppler domain as Master sampling. Slave samples follow a typical interferometric pattern. The pattern shows components ($I$ and $Q$) oscillating with a period of ≈108 s. The offset between $I$ and $Q$ indicates superimposed variations with a period much longer than the shown interval. The short-period oscillations relate to reflected contributions, and the long-period variations relate to direct contributions. A quantitative verification that takes the airfield height into account is provided in section 4.2.

### 3.3. Airborne Reflection Event

[27] Reflection event PRN 2—12 October 2010 11 h, 00 min was recorded during a straight flight over the lake starting at Bregenz {1} heading to Ludwigshafen {6}. During this event, the satellite (PRN 2) is descending at elevations between 17° and 6°. Master samples confirm again a proper phase tracking of the direct signal. They show maximum $I$ component and vanishing $Q$ component (Figure 6, top panel).

[28] The $I$ component decreases when elevation reaches 6° but still exceeds the $Q$ component that is at noise level. By contrast to the on-ground event, the relative delay during the airborne event significantly exceeds 0.1 chip. It has to be tracked in real-time otherwise Slave sampling of the reflected waveform fails. The following model is implemented for open-loop tracking

$$\Delta\tau = \frac{2(H_R - S)}{c_0} \sin E. \tag{4}$$

[29] Real-time navigation solutions of the GORS receiver provide the receiver height $H_R$ and the elevation $E$ of the tracked satellite. An a priori lake level $S$ = 440 m (WGS-84) is assumed for Lake Constance. The delay $\Delta\tau$ is adjusted using in-/decrements with 0.1 chip minimum step size given by the resolution limit. Tracking starts from $\Delta\tau = 0$ with an initial step at the beginning of the event. A zero reset of $\Delta\tau$ before tracking starts is crucial. Unfortunately, for many events in these first receiver flights, a tracking error $\delta\tau$ was introduced when $\Delta\tau$ was not reset to zero. Values $\Delta\tau$ set during the example airborne event are plotted in Figure 6 (middle panel). For the shown event, tracking is correct. According to a comparison with calculations in postprocessing, the tracking error $\delta\tau$ is below the resolution limit.

[30] A 36 s interval of Slave samples ($I$ and $Q$) is shown in Figure 6 (bottom panel). During this short interval, an interferometric pattern is resolved. Its interpretation is clearly more complex for the airborne event than for the on-ground event. Oscillation periods change rapidly within this interval. The assignment of direct and reflected contributions requires a better understanding of variations in $\varphi_1$ and $\varphi_2$. The following section provides detailed models as part of the altimetric method applied in postprocessing.

## 4. Altimetric Method

[31] GNSS signals in general are sensitive to variations of the optical phase path between transmitter and receiver. Changes in the direct path to the Master antenna are corrected in Master and Slave observations in real time. Interferometric changes received at the Slave antenna are corrected in postprocessing. Within correction, the specular height can be estimated as a model parameter. The method description starts modeling phase rates characteristic for direct and reflected contributions. Separation of the

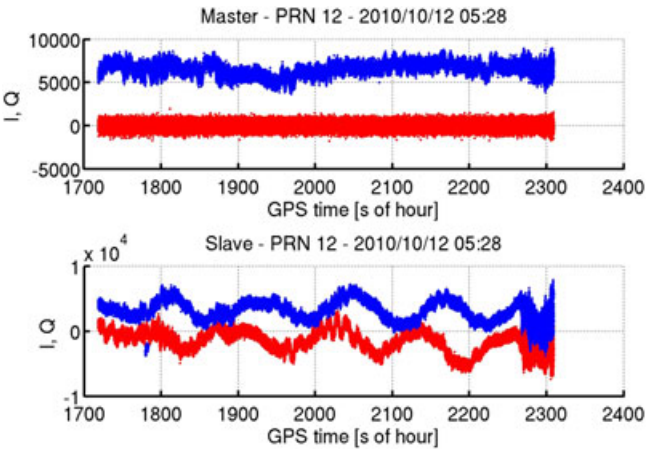


**Figure 5.** Results of Master sampling (top panel) and Slave sampling (bottom panel) for the event on ground (start 5 h, 28 min), $I$ (blue) and $Q$ (red) components are plotted.

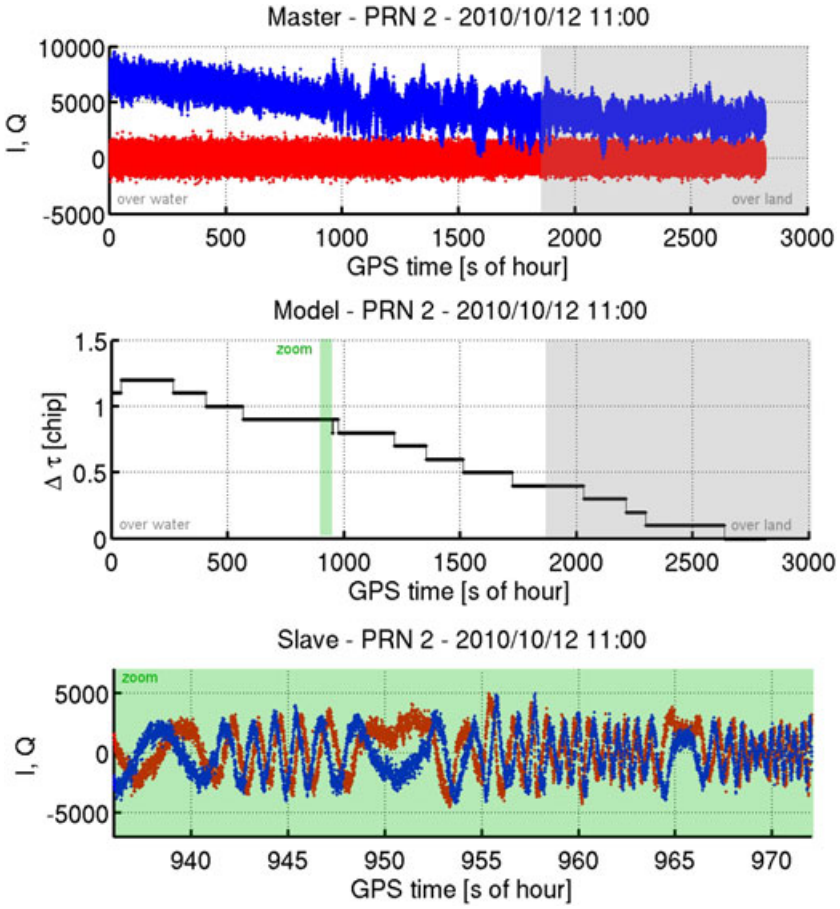


**Figure 6.** Results of (top panel) Master sampling, (bottom panel) Slave sampling, and (middle panel) code delay model used in open-loop tracking for an airborne reflection event (start 11 h, 00 min). Samples split up to $I$ (blue) and $Q$ (red) components. Reflections over land are disregarded (shaded in gray). Interferometric oscillations are shown in a 36 s interval of Slave samples (shaded in green). Discontinuities in the delay model arise from the 0.1 chip resolution limit.

reflected contribution thus is described based on dedicated filtering. The crucial step of specular height estimation follows at the end of the method description.

### 4.1. Phase Path Model

[32] The direct signal is tracked at the Master antenna's position. Direct contributions to $\gamma_{\mathrm{slv}}$ are described with the path model $\varphi_1$, introduced in equation (3). In the following, $\varphi_1$ is the baseline model. It depends on the line-of-sight vector $\vec{e}$ to the satellite (with unit length) and the antennas' baseline vector $\vec{b}$. Both parameters are defined in Figure 2. The model reads

$$\begin{aligned}\varphi_1(t) &= \frac{1}{\lambda}\left[D_{\mathrm{slv}}(t) - D_{\mathrm{mst}}(t)\right] \\ &= \frac{1}{\lambda}\vec{e}(t)\cdot\vec{b}(t) \\ &= \frac{1}{\lambda}\vec{e}(t)\cdot\left(\mathbf{R}(t)\vec{B}\right),\end{aligned} \tag{5}$$

where $\lambda$ is the L band carrier wavelength and $\mathbf{R}$ is the rotation matrix for yaw, pitch, and roll correction of baseline vector $\vec{B}$ given in an airship body frame. Roll, pitch, and yaw angles were recorded during the flight using inertial navigation. Baselines $\vec{B}$ from Master antenna to Slave antennas (RHCP and LHCP, respectively) are known from specifications of the antenna mount and have equal lengths ($16 \pm 3$ cm). The given uncertainty of 3 cm accounts for unknown phase center variations.

[33] Reflected contributions to $\gamma_{\mathrm{slv}}$ are described by a combined path model $\varphi_1 + \varphi_2$, introduced in equation (3). In addition to the baseline model $\varphi_1$, the so-called altimetric model $\varphi_2$ which depends on the specular height is necessary. Trial heights $H^j$ of the reflecting surface are introduced in a forward modeling of $\varphi_2$ for later inverse height estimation

$$\varphi_2(H^j, t) = \frac{1}{\lambda}\left[R_{\mathrm{slv}}(H^j, t) - D_{\mathrm{slv}}(t)\right].$$

[34] A ray tracing tool provides the direct path $D_{\mathrm{slv}}$ and multiple trials of the reflected paths $R_{\mathrm{slv}}$ allowing for refraction in the neutral atmosphere. Paths are adjusted by meteorological parameters (temperature, pressure, and specific humidity) provided by reanalysis products of ECMWF (European Center for Medium-range Weather Forecast). Rays considered for the altimetric method are shown in Figure 7.

[35] A local spherical approximation of the WGS-84 ellipsoid allows to link concentric spheres' radii to ellipsoidal trial heights $\rho^j = R_c + H^j$, where $R_c$ is the radius of the

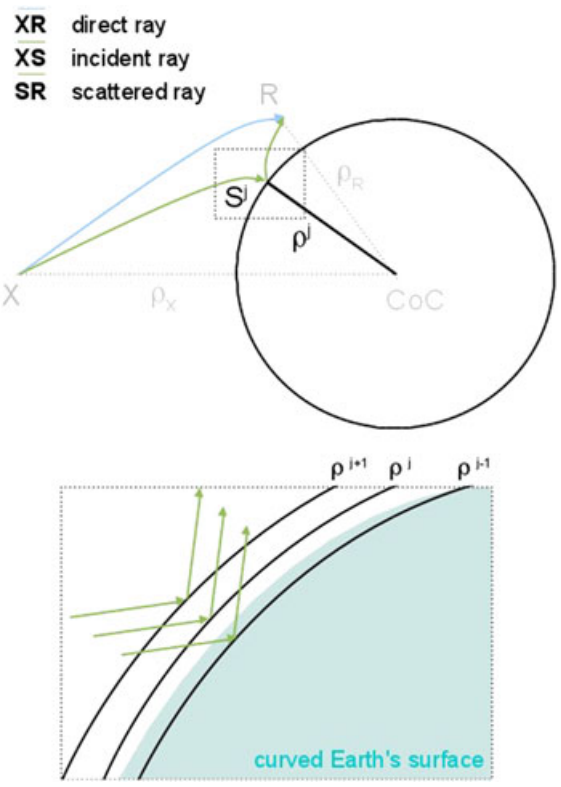


**Figure 7.** Concept of altimetric ray tracing. The path $D_{slv}$ refers to the direct ray. The path $R_{slv}$ refers to incident and scattered rays. Positions of transmitting antenna (X), receiving antenna (R) and specularly reflecting point ($S^j$) are regarded. Different spherical surface levels (trial heights) with radii $\rho^j$ are assumed (zoom). These levels are adjusted to WGS-84 ellipsoid. The adjusted reference sphere defines the common Center of Curvature (CoC).

reference sphere. In this approximation, the altimetric phase model can be written in a linear height parametrization

$$\varphi_2(H^j, t) \approx m(t)\,\Delta H^j + \varphi_2(H_S, t), \tag{6}$$

where $m(t)$ denotes the time-dependent altimetric coefficient. Trial heights $H^j = H_S + \Delta H^j$ are constant in time. They contain a departure $\Delta H^j$ from the true specular height $H_S$. Important aspects of the model, such us linearity in the departures, have been discussed in *Semmling et al.* [2012]. Aspects such as the Earth's curvature, tropospheric/ionospheric refraction, precision of transmitter orbits, and phase wind-up effects have been discussed for a ground-based scenario in *Semmling* [2012]. Aspects that similarly affect direct and reflected paths, e.g., the relativistic effects due to the inertial rotation of the Earth-fixed frame (Sagnac Effect), are disregarded.

[36] A simplified model is useful to link the most important parameters of reflection events: the transmitter elevation $E$, the receiver height $H_R$, and the specular height $H_S$. It reads

$$\varphi_2(H_S, t) \approx \frac{2}{\lambda}\,[H_R(t) - H_S]\,\sin E(t). \tag{7}$$

[37] This approximation omits parameters such as the Earth's curvature and atmospheric refraction. Although insufficient for precise altimetry, it is important to discuss modelled effects below.

### 4.2. Filtering and Spectral Analysis

[38] For the on-ground reflection event (PRN 12—12 October 2010 5h, 36 min) as well as for a typical airborne event (PRN 2—12 October 2010 11 h, 00 min), direct and reflected contributions occur in Slave observations. The phase rate $d\varphi/dt$ is calculated based on models $\varphi_1$ (direct contribution) and $\varphi_1 + \varphi_2$ (reflected contribution). Doppler shift is defined using phase rates $f := -\dot{\varphi} = -d\varphi/dt$ where a negative sign is chosen to retain the physical meaning of Doppler shift: a signal path decrease ($\dot{\varphi} < 0$) implies a blue shift ($\Delta f > 0$) and signal path increase ($\dot{\varphi} > 0$) implies a red shift ($\Delta f < 0$).

[39] In general, absolute values $|f_1|$ are significantly smaller than $|f_1 + f_2|$ (Figures 8 and 9, top panels).

[40] For the airborne event, a high-pass filter is used to remove direct contributions well below the threshold of 100 mHz. A running mean of Slave samples with a 10 s window

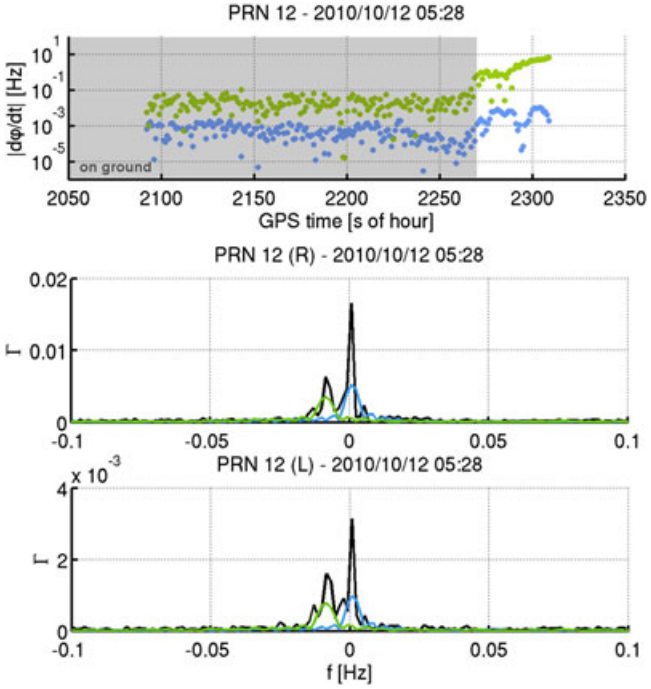


**Figure 8.** Contributions for the event on ground starting at 5 h, 28 min. (top panel) Modeled absolute Doppler values in logarithmic scale versus GPS time. Models $|f_1|$ in blue and $|f_1 + f_2|$ in green refer to direct and reflected contributions, respectively. Note that modeled values are based on observations of the airship's trajectory and attitude which introduce noise to model calculations. Only epochs on ground are regarded (gray shaded), first epochs are missing as attitude recording starts after reflection event recording. Airship's lift-off is detected by a significant increase of $|f_1 + f_2|$. (middle and bottom panels) Spectra of RHCP/LHCP data (black), direct and reflected peaks are validated with modeled spectra (blue and green). The spectra are zoomed to frequencies below 100 mHz.

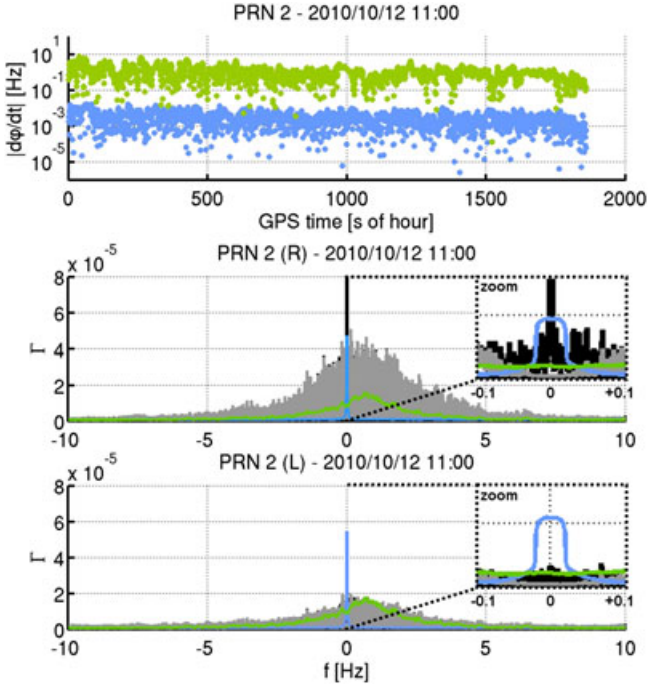


**Figure 9.** Contributions for the airborne event starting at 11 h, 00 min. (top panel) Modeled absolute Doppler values in logarithmic scale versus GPS time. Models $|f_1|$ in blue and $|f_1 + f_2|$ in green refer to direct and reflected contributions, respectively. (middle and bottom panels) Spectra of RHCP/LHCP raw data (black), direct and reflected peaks are validated with modeled spectra (blue and green). The spectra show frequencies below 10 Hz. An additional zoom (frequencies below 100 mHz) focuses on the removal of direct contributions in filtered observations (gray). To prevent complete overlap in the spectra, a running-mean filter is applied to modeled spectra leaving smoothed curves. It is applied only for the plots, the models used for ongoing retrieval are not smoothed.

is calculated to obtain components $I_{10s}$, $Q_{10s}$. These components are subtracted from $I_{slv}$, $Q_{slv}$ leaving a filtered phasor

$$\gamma_{flt} := [I_{slv} - I_{10s}] + i\,[Q_{slv} - Q_{10s}]\,. \tag{8}$$

[41] Thus, direct contribution need not be considered, and the former model of Slave observations, equation (2), simplifies to

$$\gamma_{flt} = |\gamma_{rfl}|\, e^{-i[\phi_1 + \phi_2(H_S)]}, \tag{9}$$

where $\phi$ denotes again the wrapped phase angle corresponding to path model $\varphi$. Assuming that only phase information is relevant for altimetry, the model amplitude $|\gamma_{rfl}|$ is set to an arbitrary constant. Trials of the specular height $H_S$ are used for $\phi_2$ (442 m for lake level and 455 m for airfield level in WGS-84).

[42] In addition to phasor analysis in the time domain, spectrum analysis provides the Doppler distribution in the frequency domain. The spectrum is defined by the Fourier amplitude

$$\Gamma(f) := \frac{1}{N} |\mathfrak{F}\{\gamma\}(f)|\,. \tag{10}$$

[43] The Fourier transformation $\mathfrak{F}\{\}$ acts on the phasor $\gamma$. For normalization, the factor $1/N$ is added with $N$ being the sum of $\Gamma(f)$ over all frequencies. This normalization guarantees that spectral peak amplitude is limited $\hat{\Gamma}(f) < 1$. Only in the limit of pure specular reflection it reaches one, as shown later in this paper, equation (21).

[44] Spectra for the ground event and the airborne event are shown in Figures 8 and 9 (middle panels RHCP data, bottom panels LHCP data). Each plot contains direct contribution models $\Gamma_1$ (blue), reflected contribution models $\Gamma_{1+2}$ (green), and Slave observations $\Gamma_{slv}$ (black). In general, direct peaks are found in observations close to $f = 0$. They agree in peak location with models $\Gamma_1$ (blue). For the airborne event, the direct peak in RHCP data is significantly higher than in LHCP data. This can be explained by initial polarization (RHCP) which persists for the direct signal. Observations are filtered $\Gamma_{flt}$ (gray) to remove direct peaks, as shown in the insets of Figure 9. For the ground event, the filter is not applied as reflected peaks are below the threshold (100 mHz).

[45] Reflected peaks are found with significant Doppler shifts. They also agree in peak location with according models $\Gamma_{1+2}$ (green). Characteristics of ground and airborne data are different. For the ground event, the constant height difference $H_R - H_S$ ($\approx$10 m) is responsible for rather sharp peaks (full width at half maximum $\approx$0.01 Hz). For the airborne event, a variable height difference $H_R - H_S$ (between 554 and 650 m) is responsible for much broader peaks (full width at half maximum $\approx$3 Hz). The agreement of modeled and observed reflected peaks justifies the correction of variations

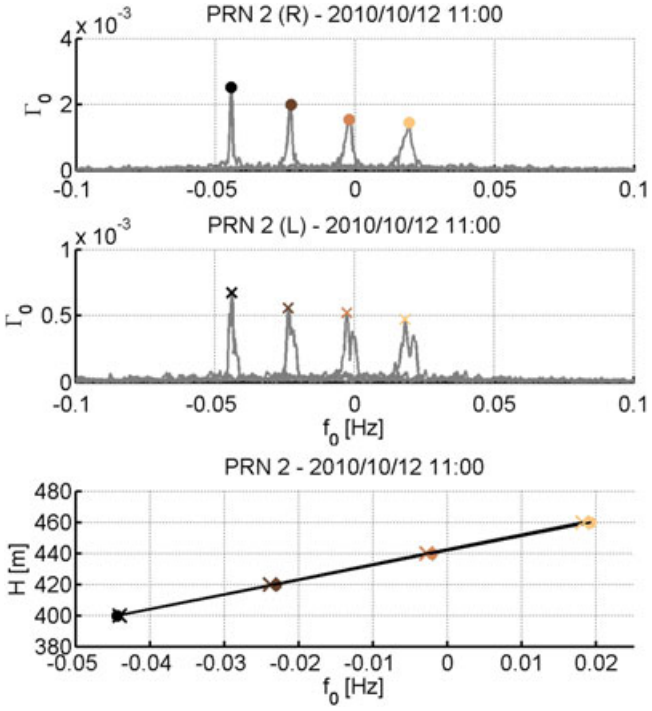


**Figure 10.** Surface height estimation for the airborne event. (top/middle panel) Residual spectra for RHCP/LHCP data, each panel contains four spectra with color-coded peaks corresponding to the different trial heights. (bottom panel) Linear fit of trial heights and Doppler residuals retrieved from spectra above.

**Table 1.** Retrieved Doppler Residuals for the Airborne Event (PRN 2)[a]

| $H^j$ | (m) | 400 | 420 | 440 | 460 |
|---|---|---|---|---|---|
| $f_0$ (RHCP) | (mHz) | –44 | –23 | –2 | +19 |
| $f_0$ (LHCP) | (mHz) | –44 | –24 | –3 | +18 |

[a]The four residuals correspond to four trial heights.

in filtered observations using the model $\gamma_{1+2}(H_s)$ as is done in the first step of specular height estimation.

### 4.3. Specular Height Estimation

[46] Three principal steps are used to estimate the specular height: (1) Doppler correction, (2) residual Doppler retrieval, and (3) a linear fit.

[47] Doppler variation is corrected by counter-rotation of the filtered phasor observation through trial phasor models

$$\gamma_0^j(H^j, t) = \gamma_{1+2}^j(H^j, t)\, \gamma_{\mathrm{flt}}(t)^*. \tag{11}$$

[48] Doppler correction results in residual phasors $\gamma_0^j$ specified by trial heights $H^j$.

[49] Doppler retrievals after correction have been described in *Semmling et al.* [2012]. A short review on spectral retrieval is given here with the residual Doppler $f_0$ determined from the peak position in the residual spectrum

$$f_0^j = f\left(\hat{\Gamma}_0^j\right), \tag{12}$$

where $\hat{\Gamma}_0^j$ is the spectral peak corresponding to the phasor $\gamma_0^j$.

[50] If retrievals $f_0^j$ are correlated with trial heights $H^j$, a linear fit can be applied based on the following equation

$$H^j(f_0^j) = \overline{\dot{m}(t)}^{-1} f_0^j + H_s. \tag{13}$$

[51] This relation refers back to phase residuals $\varphi_0$ that are connected to height deviation $H^j - H_s$ via the altimetric coefficient $m(t)$ which describes the sensitivity of $\varphi_0$ to height deviation. In case of Doppler residuals, a linear fit ($H(f_0)$) provides the undetermined parameters in equation (13): the inverse mean time derivative of the altimetric coefficient $m(t)$ and the specular height $H_s$. To illustrate the concept here, it is applied to the airborne event of PRN 2. Residual spectra $\Gamma_0$ for RHCP/LHCP data are shown in Figure 10 (top/middle panel).

[52] Doppler residuals $f_0$ are retrieved from the indicated peak position. Peaks are color-coded from dark to light brown with increasing trial height. Small differences between RHCP and LHCP residuals are detected (Table 1).

[53] Correlation of these residuals $f_0^j$ with trial heights $H^j$ and the linear fit $H(f_0)$ is shown in the bottom panel of Figure 10. Estimates $H_s$ at $f_0 = 0$ are 441.9 m (RHCP) and 442.7 m (LHCP).

[54] The deviation between RHCP and LHCP estimates of 0.8 m is significant. The formal precision $\delta H$ for this airborne event is 0.4 m. A corresponding equation has also been derived in previous work [*Semmling et al.*, 2012] assuming singular residual peaks

$$\delta H = \left| \frac{1}{T\,\overline{\dot{m}}} \right|. \tag{14}$$

[55] This formal precision depends on mean time derivative of $m(t)$ and observation time $T$ used for spectral retrieval, which is $T = 1860$ s for this event. In contrast to a singular residual peak that indicates complete Doppler correction, broad residual peaks in Figure 10 indicate unmodeled effects that influence the results as it is discussed later.

## 5. Results

[56] In total, 93 reflection events were recorded during the two flights shown in Figure 1. Unfortunately, the number of useful airborne events was reduced by a tracking error $\delta\tau$ as has been described in section 3.3. For 10 events (11%), tracking was sufficient to retrieve Doppler residuals. Large surface extensions at the lake's eastern end provide specular reflection conditions with few land multipath sources. Height estimates of three eastern events with reflection tracks shown in Figure 11 (first panel) are compared in a case study.

[57] These events fulfill two requirements: their Doppler residuals are correlated with trial heights, i.e., a linear fit $H(f_0)$ can be applied, and their duration ($T > 1000$ s) offers a precision $1/T$ of Doppler retrieval in the submillihertz range (Table 2).

[58] Two events (PRN 2 and PRN 5) are at grazing elevations ($< 20°$) and the third event (PRN 24) is at higher slant elevations ($> 20°$). Grazing events (PRN 2 and PRN 5) are correctly tracked ($\delta\tau < 0.1$ chip). A considerable tracking error ($\delta\tau = -0.7$ chip) caused by false initial settings occurs for PRN 24. For the third event, the altimetric method applies although the reflected waveform is sampled on its leading edge with a constant offset of 0.7 chip before the specular delay.

### 5.1. Lake Level Estimates

[59] The same method applied for PRN 2 in the last section also applies for PRN 5 and PRN 24. Specular heights are interpreted as estimates of a constant lake level and are validated with reference lake level below. Estimates for RHCP/LHCP data are given in Table 3 (row 1/2). The corresponding formal precision is added in the same Table (row 3).

[60] Reference level is additionally taken from tide gauges and transformed to WGS-84

$$H_{\{k\}} = G_{\{k\}} + h_{\{k\}}, \tag{15}$$

where the index $\{k\} = 2, 3, 5$, and 7 specifies the tide gauge location. Geoid heights $h_{\{k\}}$ observed by tide gauges refer to mean sea level at Amsterdam (ü. NN). The corresponding geoid correction $G_{\{k\}}$ is determined with the GCG-05 model for the location's latitude $\Phi_{\{k\}}$ and longitude $\Lambda_{\{k\}}$.

**Table 2.** Parameter for the Three Events[a]

| | | PRN 2 | PRN 5 | PRN 24 |
|---|---|---|---|---|
| $T$ | (s) | 1860 | 1759 | 1572 |
| $1/T$ | (mHz) | 0.5 | 0.5 | 0.6 |
| $E$ | (deg) | 6–17 | 4–12 | 26–37 |
| $\delta\tau$ | (chip) | >0.1 | >0.1 | –0.7 |
| $\overline{\varphi_\chi}$ | (cm) | 24 | 26 | 10 |

[a]Row 1: Events' duration, Row 2: Precision of Doppler retrieval, Row 3: Range of elevation angle from east to west, Row 4: Tracking error of slave sampling, and Row 5: Mean value of water-vapor related path model.

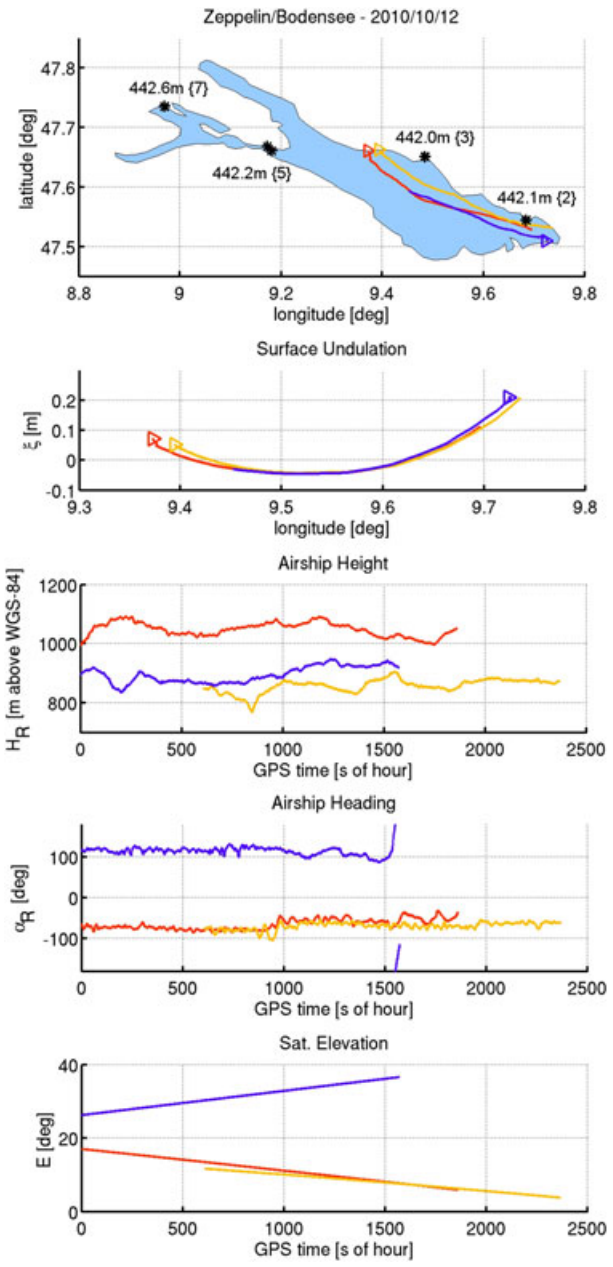


**Figure 11.** Airborne reflection events of PRN 2 (red), PRN 5 (yellow), and PRN 24 (blue). (first panel) Reflection tracks on the lake surface. The tracks follow the airship's heading, their ends are marked with triangles. For PRN 2 and PRN 5, they run in western direction, for PRN 24 in eastern direction. Tide gauge locations are marked with black stars. Mean reference lake level (WGS-84) is added next to the marker. (second panel) Surface undulation versus longitude, tracks' ends are marked with triangles. Undulation is modeled according to the Geoid model (GCG-05), lake level $H_{\{3\}}$ at Friedrichshafen is used as reference. (third panel) Airship height versus GPS time. (fourth panel) Airship heading versus GPS time. (fifth panel) Satellite elevation versus GPS time. The three events are spread over 4.5 h starting at 11 h, 00 min (PRN 2), 13 h, 09 min (PRN 5), and 15 h, 00 min (PRN 24) GPS time, i.e., events are not at the same time even if their plot shows the same second of hour.

Values $H_{\{k\}}$ are added to panel 1 of Figure 11. Modern tide gauge techniques provide hourly data that meet 1 cm accuracy requirements [*Martín-Míguez et al.*, 2012]. Tide gauge observations $h_{\{k\}}$ vary less than 3 cm during the 4.5 h period that encloses the three events. Disregarding temporal changes, the mean value of $h_{\{k\}}$ is assumed with an accuracy better than 3 cm. With GCG-05's accuracy being better than 4 cm [*Brüggemann*, 2005], reference level $H_{\{k\}}$ is determined with an accuracy better than 7 cm, which is sufficient to validate estimates with decimeter precision. Spacial variations of reference level occur due to geoid undulations.

[61] Deviations $\Delta H = H_S - H_{\{3\}}$ of estimates (RHCP and LHCP) from nearby reference level $H_{\{3\}}$ are added in Table 3 (rows 4 and 5). Although formal precision $\delta H$ is similar for the three events, the method performs differently. Both estimates of PRN 5 agree with reference level taking account of formal precision. Deviations exceeding $\delta H$ occur for PRN 2 (LHCP) and for both estimates of PRN 24. Effects with Doppler shifts that either have already been corrected or can be corrected by additional model predictions are discussed below.

### 5.2. Corrected Doppler Shift

[62] The wide distribution of observed Doppler (reflected peak in Figure 9) has been corrected with models $\varphi_1$ and $\varphi_2$ yielding a much narrower distribution of residual Doppler (Figure 10, top and middle panels). Corrected effects are quantified with respect to the corresponding Doppler shift $f = -d\varphi/dt$. The altimetric Doppler $f_2$ and the baseline Doppler $f_1$ are now considered separately for the three example events. Mean and standard deviation, $\bar{f}$ and std($f$), are given respectively in Table 4.

[63] Doppler shifts $f_2$ are the most important. According to the approximation of $\varphi_2$ in equation (7), receiver height $H_R$ and transmitter elevation $E$ are the dominant parameters in the altimetric path model. Plots of $H_R$ and $E$ are added in Figure 11 (third and fourth panels). The positive sign of $\overline{f_2}$ is characteristic for setting events ($E$ decreasing for PRN 2 and PRN 5) and the negative sign for the rising event ($E$ increasing for PRN 24). The large variability of $f_2$ is related to variations of $H_R$ (cf. std($f_2$) and std($H_R$) in Table 4). For PRN 24, it is particularly large due to higher elevation angles.

[64] Doppler shifts $f_1$ are less important. The mean $\overline{f_1}$ is almost negligible due to the short baseline between antennas. The airship heading, plotted in Figure 11 (fifth panel), is an important attitude parameter that affects significantly the baseline model. The variance indicated by std($f_1$) is relatively large due to the variable airship heading (cf. std($\alpha_R$) in Table 4).

**Table 3.** Altimetric Results[a]

| | | PRN 2 | PRN 5 | PRN 24 |
|---|---|---|---|---|
| $H_S$ (RHCP) | (m) | 441.9 | 441.7 | 442.9 |
| $H_S$ (LHCP) | (m) | 442.7 | 442.1 | 442.8 |
| $\delta H$ | (m) | ±0.4 | ±0.6 | ±0.6 |
| $\Delta H$ (RHCP) | (m) | –0.1 | –0.3 | +0.9 |
| $\Delta H$ (LHCP) | (m) | +0.7 | +0.1 | +0.8 |

[a]Rows 1 and 2: Lake level estimates for RHCP/LHCP data with model's standard configuration. Row 3: Formal precision of estimates. Rows 4 and 5: Deviation of RHCP/LHCP estimates from nearby reference level at Friedrichshafen.

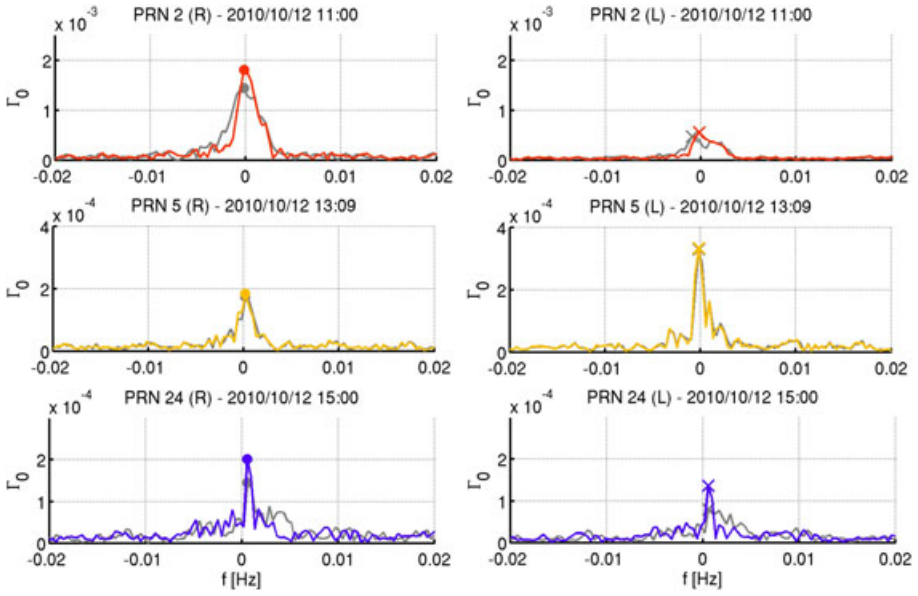


**Figure 12.** Response to undulation correction for the three events PRN 2 (red), PRN 5 (yellow), and PRN 24 (blue). RHCP/LHCP spectra are considered (left/right columns). Corrected spectra are color-coded. Uncorrected spectra with constant height are gray. The peak is indicated by circles/crosses (RHCP/LHCP).

[65] Another Doppler shift which is related to refraction of atmospheric water vapor has been corrected. It is modeled along paths $R$ and $D$, cf. $\varphi_2$ in equation (3), and derived from ray tracing results

$$\varphi_\chi = \varphi_2(H_s, t, \chi) - \varphi_2(H_s, t, \chi = 0), \tag{16}$$

where $\varphi_2$ is calculated with the ray tracing tool for two different configurations. In standard configuration, water vapor refraction is modeled. It is quantified by the specific humidity $\chi$ as has been described for ground-based experiments [*Semmling*, 2012]. In dry configuration, $\chi$ is set to zero ignoring any water vapor refraction that occur along paths $R$ and $D$. For height estimation, the standard configuration of the ray tracing tool is used. The specific humidity $\chi$, with 0.5°×0.5° spatial resolution and 6 h temporal resolution, is taken from vertical profiles of operational ECMWF analysis. Such profiles have a significant uncertainty $\delta\chi$. For the described events, the relative uncertainty $\delta\chi/\chi$ is about 10%. The mean of $\varphi_\chi$ lies between 10 and 26 cm dependent on satellite elevation (cf. $\overline{\varphi_\phi}$ in Table 2). The total Doppler shift induced by water vapor $f_\chi = -d\varphi_\chi/dt$ is calculated. Mean and standard deviation are added to Table 4. The variance is induced mainly by changes of the airship height. The elevation angle is also an important parameter for the water vapor effect. At grazing elevation (PRN 2 and PRN 5), $\overline{f_\chi}$ is 10 times larger than at higher slant elevation (PRN 24).

**Table 4.** Mean and Standard Deviation of Modeled Doppler Shifts and Flight Parameters for the Three Events[a]

| | | PRN 2 | PRN 5 | PRN 24 |
|---|---|---|---|---|
| $\overline{f_2}$ | (mHz) | +552.4 | +316.2 | –559.7 |
| $\overline{f_1}$ | (mHz) | +0.2 | +0.2 | 0.0 |
| $\overline{f_\chi}$ | (mHz) | –1.0 | –1.0 | +0.1 |
| $\overline{f_\xi}$ | (mHz) | +0.1 | +0.2 | –0.9 |
| std($f_2$) | (mHz) | 1257 | 1107 | 3116 |
| std($f_1$) | (mHz) | 6.0 | 8.0 | 6.5 |
| std($f_\chi$) | (mHz) | 1.4 | 2.8 | 0.5 |
| std($f_\xi$) | (mHz) | 0.5 | 0.5 | 1.2 |
| std($H_R$) | (m) | 23.5 | 23.0 | 27.9 |
| std($\alpha_R$) | (deg) | 12.6 | 8.9 | 32.2 |

[a]Rows 1 and 5: Doppler based on the altimetric model $\varphi_2$. Rows 2 and 6: Doppler based on the baseline model $\varphi_1$. Rows 3 and 7: Doppler based on the water vapor model $\varphi_\chi$. Rows 4 and 8: Doppler based on the undulation model $\varphi_\xi$. Rows 9 and 10: Standard deviation of airship height and airship heading.

### 5.3. Undulation Doppler Shift

[66] Doppler shifts $f_2$, $f_1$, and $f_\chi$ have already been corrected for retrieval. The described events last for more than 1000 s. Variations of lake level along the reflection track are important for altimetry but have been ignored, so far. During such events, the airship covers considerable distances over Lake Constance where geoid undulations of several decimeter occur (Figure 11, first panel). A time-dependent undulation along the track $\xi(t)$ is easily incorporated into the altimetric model $\varphi_2$ which is linear in the surface height, cf. equation (5),

$$\begin{aligned}\varphi_2(H_s, t, \xi(t)) &= \varphi_2(0, t) + \lambda^{-1}\, m(t)\, H_s + \varphi_\xi(t) \\ &= \varphi_2(0, t) + \lambda^{-1}\, m(t)[H_s + \xi(t)] \\ \varphi_\xi(t) &= \lambda^{-1}\, m(t)\, \xi(t),\end{aligned} \tag{17}$$

**Table 5.** Parameters of Residual Spectra[a]

| | | PRN 2 | PRN 5 | PRN 24 |
|---|---|---|---|---|
| $\Delta f$(RHCP) | (mHz) | 0.0 | 0.0 | 0.0 |
| $\Delta f$(LHCP) | (mHz) | 0.8 | 0.0 | 0.0 |
| $\hat{\Gamma}_0(H_{\{3\}})$ (RHCP) | $10^{-4}$ | 15.5 | 1.8 | 1.5 |
| $\hat{\Gamma}_0(H_{\{3\}})$ (LHCP) | $10^{-4}$ | 5.0 | 3.3 | 0.8 |

[a]Rows 1 and 2: Doppler shifts as response to undulation correction. Rows 3 and 4: Peak amplitude of uncorrected residuals.

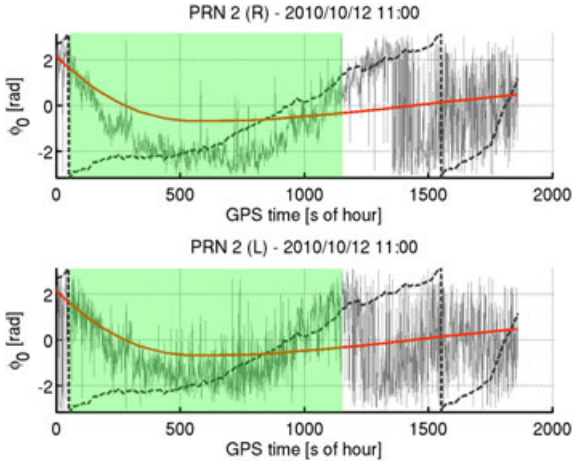


**Figure 13.** Phase residuals for PRN 2 considering RHCP/LHCP data (top/bottom panel). Residual data $\phi_0$ (gray) have been interpolated to a 1 Hz sampling. The modeled bias $\phi_\chi$ (dashed line) and the additional bias $\phi_\xi$ (red solid line) are plotted for comparison. An interval (green shaded) with continuous phase residuals is selected for interpretation.

where $H_S + \xi(t)$ is the undulation-corrected height based on the constant value $H_S$. The optimum surface model considers both: the reference height $H_{\{3\}}$ provides the constant value, the geoid model $G$ provides the undulation. The undulation reads

$$\xi(t) = G(\Lambda_S(t), \Phi_S(t)) - G_{\{3\}}, \tag{18}$$

where the index S specifies the location of the specular reflection track in longitude, latitude ($\Lambda$, $\Phi$) and $G_{\{3\}}$ is the geoid at the reference point. The undulation for the three example events is similar. It passes a minimum at mid longitudes of the reflection tracks (Figure 11, second panel). The undulation amplitude reaches a maximum of 25 cm. The Doppler shift $f_\xi = -d\varphi_\xi/dt$ induced by undulation is modeled. Mean and standard deviation are added to Table 4. The Doppler shift clearly depends on the elevation angle. At grazing elevation (PRN 2 and PRN 5), $\overline{f_\xi}$ is more than four times smaller compared to the higher slant elevation (PRN 24). The mean Doppler $\overline{f_\xi}$ is only significant for PRN 24 taking into account the Doppler precision achieved with spectral retrieval (Table 2).

[67] Effects of surface undulation and receiver height variation can hardly be distinguished. A simplified model of $\varphi_2$ has been introduced in equation (7). Adding the undulation term $\xi$, the model reads

$$\varphi_2(\xi(t)) \approx \frac{2}{\lambda}\,[H_R(t) - H_S - \xi(t)]\,\sin E(t). \tag{19}$$

[68] In this case, surface undulation and receiver height variations are completely correlated. A contribution $\xi$ can be interpreted either as an increase in $H_S$ or as an decrease in $H_R$. Even if surface undulation is corrected, the accuracy of $H_S$ is still restricted by the uncertainty of $H_R$.

### 5.4. Residual Doppler Shift

[69] After Doppler correction, the peak width of Doppler distribution is significantly reduced (Figure 10). The peaks plotted there have a Doppler shift proportional to constant trial heights $H^j$. This Doppler shift is a first-order response of spectral retrieval. Changes of the peak shape (increasing peak width from left to right in Figure 10) are regarded as a higher-order response of spectral retrieval.

[70] In the idealized case of complete Doppler correction, residuals are expressed as

$$\gamma_0(\Delta H, t) = |\gamma_0| e^{-2\pi i f_0 t}, \tag{20}$$

with constant amplitude $|\gamma_0|$ and constant residual Doppler $f_0$. The corresponding spectrum,

$$\Gamma_0 = \frac{|\gamma_0|}{N}\delta(f - f_0), \tag{21}$$

is dominated by the *Dirac-δ-distribution* $\delta(f - f_0)$ which is zero everywhere except for the singular residual peak $\hat{\Gamma}_0$ at $f_0$. In practice, a broader peak shape occurs indicating insufficient Doppler correction.

[71] The response of spectral retrieval to $\xi(t)$ is examined for the three events in Figure 12, regarding RHCP and LHCP data, respectively.

[72] Undulation-corrected spectra $\Gamma_0(H_{\{3\}} + \xi)$ and uncorrected spectra $\Gamma_0(H_{\{3\}})$ are compared. The first-order response given by the Doppler shift of the peak position is determined

$$\Delta f = f_0(H_{\{3\}} + \xi) - f_0(H_{\{3\}}), \tag{22}$$

where both residuals $f_0$ are obtained by spectral retrieval according to equation (12). Shifts $\Delta f$ are summarized in Table 5.

[73] In general, a first-order response $\Delta f$ to undulation correction is not detected. The shift detected for LHCP data of PRN 2 is an exception. A higher-order response given by changes in the peak shape occurs for PRN 24.

[74] The higher-order response cannot be explained by the idealized model of a singular peak, equation (21). A generalized model including the phasor amplitude $|\gamma_0|$ is required. *Fresnel coefficients* must be taken into account to quantify changes in phase and amplitude induced by surface properties as described in [*Smyrnaios et al.*, 2013]. Such a generalized model including *Fresnel coefficients* also accounts for signal polarization. Differences in residual peak amplitudes $\hat{\Gamma}_0$ reported for RHCP/LHCP in Table 5 could be explained using this model.

### 5.5. Residual Phase Shift

[75] Phase data have a higher precision than Doppler residuals. It is anticipated that the data $\phi_0 = \arg[\gamma_0]$, given by the phase argument of the residual $\gamma_0$, better resolve undulation effects. Unfortunately, phase data are often disturbed by surface roughness [*Semmling et al.*, 2012]. Out of the three events, only PRN 2 contains a segment where phase information can be retrieved. Wrapped phase residuals $\phi_0$ for RHCP/LHCP are plotted in Figure 13 (top/bottom panel), respectively.

[76] In the selected interval (green shaded), RHCP and LHCP residuals are largely in agreement. To quantify the different effects, the phase range in this interval is determined calculating distances $\Delta\phi$ between local phase minimum and maximum. The phase range $\Delta\phi_0$ is 4.8 and 4.0 rad for RHCP and LHCP data. These values are slightly below

the range of the water vapor related effect $\Delta\phi_\chi$ with 4.9 rad but considerably above the range of the undulation effect $\Delta\phi_\xi$ with 2.4 rad. This means that phase residuals cannot be adequately described by the undulation effect in this event. Model accuracy needs to be improved to resolve the undulation effect in phase residuals.

## 6. Summary

[77] The study is based on flights with a zeppelin airship over Lake Constance. Flight transects between eastern and western ends of the lake (64 km) were conducted with changing heights (300–800 m) above the lake surface. Interferometric observations of direct and reflected GNSS signals were acquired with the airborne receiver setup. Relative code delays between direct signal and reflection are tracked in a Master-Slave sampling. An uplooking Master antenna ensures independent tracking of the direct signal. Two down-looking Slave antennas (RHCP/LHCP) point to reflected signals. Direct contributions of Slave observations are removed with a filter.

[78] The altimetric method is described for the airborne event of PRN 2. The variance of the altimetric path leads to a broad reflection peak in the Slave spectrum (Figure 9). The peak is centered at about 0.5 Hz with a full width at half maximum of 3 Hz. Doppler correction yields Doppler residuals proportional to surface trial heights. The correlation of Doppler residuals and trial heights is used for inverse estimation of the specular height. The formal precison of estimates obtained from this spectral retrieval is in the decimeter range.

[79] In a case study, lake level estimates are obtained for three events regarding RHCP/LHCP data. These estimates are validated with tide gauge reference data. The accuracy of RHCP/LHCP estimates (10–90 cm) is worse than the formal precision (40–60 cm) in some cases. To identify model deficits, corrected effects are compared to the additional effect predicted for geoid-induced surface undulation (25 cm amplitude). The altimetric correction has the largest mean Doppler shift (316–560 mHz). For baseline correction (less than 0.2 mHz), water vapor correction (0.1–1.0 mHz), and undulation prediction (0.1–0.9 mHz), the mean Doppler shift is much smaller.

[80] Precision of Doppler residuals as the first-order response of spectral retrieval is insufficient to resolve the undulation effect. Modeling higher-order response could improve the results. The current precision, however, is unsatisfying taking into account that retracking techniques applied to the waveform of C/A code observations reach a better precision [*Rius et al.*, 2010; *Ruffini et al.*, 2004]. Phase residuals potentially have centimeter precision. A critical point for altimetry based on phase observations is their ambiguity. Doppler retrieval is not ambiguous but the reported precision (better than 1 mHz) requires a long time scale (more than 1000 s). An improved time resolution using phase data is required for future airborne or spaceborne altimetry. Here a time-resolved analysis of phase data is already presented for the event of PRN 2. Major parts of RHCP/LHCP residuals agree. A comparison shows, however, that undulation is not the dominant effect in residuals. Other effects, such as phase wind-up [*Beyerle*, 2008], have to be examined in future studies.

[81] The described altimetric method focuses on surface height estimation. Doppler correction is used but it is considerably influenced by flight parameters (airship height and heading). These variables need to be reduced (smoother flight) to improve Doppler correction in future experiments. A similar altimetric method focussing on the aircraft height can be considered. Multiple reflection events tracked simultaneously during a flight over a well-defined surface can be useful to estimate the aircraft height.

[82] In general, the use of phase retrievals is crucial to improve precision and time resolution of the altimetric method. Such phase observation can contribute to detect phenomena, like tsunamis or mesoscale ocean eddies, using GNSS reflections.

[83] **Acknowledgments.** We would like to express our sincere appreciation to Zeppelin Luftschifftechnik (ZLT) for all the support during the flight campaign. Wir sind sehr dankbar für die technische Unterstützung durch M. Ludwig und andere Kollegen der Werkstatt. Vielen Dank für die Pegeldaten, die durch die Landesanstalt für Umwelt, Messungen und Naturschutz Baden-Württemberg und das Bayerische Landesamt für Umwelt zur Verfügung gestellt wurden. We are also grateful for the provision of GPS ephemerides by R. König and other colleagues. The ECMWF is gratefully acknowledged for providing meteorological data. Hardware for the GORS receiver was provided by JAVAD GNSS. This study was funded by GFZ and DLR.

## References

Ablain, M., J. Dorandeu, P. Le Traon, and A. Sladen (2006), High resolution altimetry reveals new characteristics of the December 2004 Indian Ocean tsunami, *Geophys. Res. Lett.*, *33*, L21602, doi:10.1029/2006GL027533.

Beckmann, P., and A. Spizzichino (1987), *The Scattering of Electromagnetic Waves from Rough Surfaces*, 511 pp., Artech House, Inc., Nordwood, MA, reprint, Pergamon Press, 1963. (International Series of Monographs on Electromagnetic Waves; 4), Originally published: Oxford [Oxfordshire]; New York.

Beyerle, G. (2008), Carrier phase wind-up in GPS reflectometry, *GPS Solutions*, *13*, 191–198, doi:10.10007/s10291-008-0112-1.

Beyerle, G., K. Hocke, J. Wickert, T. Schmidt, C. Marquardt, and C. Reigber (2002), GPS radio occultations with CHAMP: A radio holographic analysis of GPS signal propagation in the troposphere and surface reflections, *J. Geophys. Res.*, *107*(D24), 4802–4815, doi:10.1029/2001JD001402.

Bilich, A., K. M. Larson, and P. Axelrad (2008), Modeling GPS phase multipath with SNR case study the Salar de Uyuni, Boliva, *J. Geophys. Res.*, *113*, B04401, doi:10.1029/2007JB005194.

Borre, K., D. M. Akos, N. Bertelsen, P. Rinder, and S. Holt Jensen (2007), *A Software-defined GPS and Galileo Receiver: A Single-Frequency Approach*, Birkhuäuser, Boston.

Brüggemann, T. (2005), Einsatz des Geoids "German Combined Quasi-Geoid 2005 (GCG05)" in der WSV, Bundesanstalt für Gewässerkunde.

Cardellach, E., C. O. Ao, M. de la Torre Juarez, and G. A. Hajj (2004), Carrier phase delay altimetry with GPS-reflection/occultation interferometry from low earth orbiters, *Geophys. Res. Lett.*, *31*, L10402, doi:10.1029/2004GL019775.

Cardellach, E., F. Fabra, O. Nogués-Correig, S. Oliveras, S. Ribó, and A. Rius (2011), GNSS-R ground-based and airborne campaigns for ocean, land, ice, and snow techniques: Application to the GOLD-RTR data sets, *Radio Sci.*, *46*, RS0C04, doi:10.1029/2011RS004683.

Chelton, D. B., J. C. Ries, B. J. Haines, L.-L. Fu, and P. S. Callahan (2001), Satellite altimetry, in *Satellite Altimetry and Earth Sciences: A Handbook of Techniques and Applications, International Geophysics Series,* vol. 69, edited by L.-L. Fu and A. Cazenave, chap. 1, pp. 1–131, Academic Press, San Diego.

Garrison, J. L., and S. J. Katzberg (2000), The application of reflected gps signals to ocean remote sensing, *Remote Sens. Environ.*, *73*, 175–187.

Ge, M., J. Douša, X. Li, M. Ramatschi, T. Nischan, and J. Wickert (2012), A novel real-time precise positioning service system: Global precise point positioning with regional augmentation, *J. Global Position. System*, *11*(1), 2–10, doi:10.5081/jgps.11.1.2.

Gleason, S., S. Hodgart, Y. Sun, C. Gommenginger, S. Mackin, M. Adjrad, and M. Unwin (2005), Detection and processing of bistatically reflected

GPS signals from low earth orbit for the purpose of ocean remote sensing, *IEEE Trans. Geosci. Remote Sens.*, *43*(6), 1229–1241.

Liebsch, G., U. Schirmer, J. Ihde, H. Denker, and J. Müller (2006), Quasi-geoidbestimmung für Deutschland, in *DVW-Schriftenreihe*, pp. 127–146, vol. 49, Wißner-Verlag GmbH & Co. KG, Augsburg, Germany.

Lowe, S. T., C. Zuffada, Y. Chao, P. Kroger, L. E. Young, and J. L. LaBrecque (2002), 5-cm-precision aircraft ocean altimetry using GPS reflections, *Geophys. Res. Lett.*, *29*(10), 1375–1378, doi:10.1029/2002GL014759.

Martín-Míguez, B., L. Testut, and G. Wöppelmann (2012), Performance of modern tide gauges: Towards mm-level accuracy, *Sci. Mar.*, *76S1*, 221–228, doi:10.3989/scimar.03618.18A.

Martín-Neira, M. (1993), A passive reflectometry and interferometry system PARIS: Application to ocean altimetry, *ESA Journal*, *17*, 331–355, Radio-Frequency Division, ESTEC, Noordwijk, The Netherlands.

Misra, P., and P. Enge (2001), *Global Positioning System- Signals, Measurements, and Performance*, 590 p., Ganga-Jamuna Press, Lincoln, Massachusetts.

Nerem, R. S., D. P. Chambers, C. Choe, and G. T. Mitchum (2010), Estimating mean sea level change from the TOPEX and Jason altimeter missions, *Mar. Geod.*, *33*, 435–446.

Nogués-Correig, O., E. Cardellach, J. Sanz Campderros, and A. Rius (2007), A GPS-reflections receiver that computes doppler/delay maps in real-time, *IEEE Trans. Geosci. Remote Sens.*, *45*(1), 156–174, doi:10.1109/TGRS.2006.882257.

Rius, A., E. Cardellach, and M. Martin-Neira (2010), Altimetric analysis of the sea surface GPS reflected signals, *IEEE Trans. Geosci. Remote Sens.*, *48*, 2119–2127.

Rius, A., et al. (2012), Altimetry with GNSS-R interferometry: First proof of concept experiment, *GPS Solutions*, *16*, 231–241, doi:10.1007/s10291-011-0225-9.

Ruffini, G., F. Soulat, M. Caparrini, O. Germain, and M. Martín-Neira (2004), The Eddy experiment: Accurate GNSS-R ocean altimetry from low altitude aircraft, *Geophys. Res. Lett.*, *31*, L12306, doi:10.1029/2004GL019994.

Semmling, A. M., et al. (2011), Detection of Arctic Ocean tides using interferometric GNSS-R signals, *Geophys. Res. Letters*, *38*, L04103, doi:10.1029/2010GL046005.

Semmling, A. M., T. Schmidt, J. Wickert, S. Schön, F. Fabra, E. Cardellach, and A. Rius (2012), On the retrieval of the specular reflection in GNSS carrier observations for ocean altimetry, *Radio Sci.*, *47*, RS6007, doi:10.1029/2012RS005007.

Semmling, M. (2012), Altimetric monitoring of Disko Bay using interferometric GNSS observations on L1 and L2, *vol. Scientific Technical Report STR12/04*, Helmholtz Centre Potsdam, GFZ German Research Centre for Geosciences, doi:10.2312/GFZ.b103-12049.

Smyrnaios, M., S. Schön, and M. Liso Nicolás (2013), Multipath propagation, characterization and modeling in GNSS, in *Geodetic Sciences - Observations, Modeling and Applications*, edited by S. Jin, pp. 99–125. InTech Europe, Rijeka, Croatia, ISBN 978-953-51-1144-3, doi:10.5772/3439.

Stosius, R., G. Beyerle, A. Helm, A. Hoechner, and J. Wickert (2010), Simulation of space-borne tsunami detection using GNSS-reflectometry applied to tsunamis in the Indian ocean, *Nat. Hazards Earth Syst. Sci.*, *10*(6), 1359–1372.

Treuhaft, R. N., S. T. Lowe, C. Zuffada, and Y. Chao (2001), 2-cm GPS altimetry over Crater Lake, *Geophys. Res. Lett.*, *22*(23), 4343–4346.

Xu, Y., J. Li, and S. Dong (2011), Ocean circulation from altimetry: Progress and challenges, in *Ocean Circulation and El Niño: New Research*, edited by J. A. Long and D. S. Wells, pp. 71–97, Nova Publishers, New York.

Zavorotny, V. U., and A. G. Voronovich (2000), Scattering of GPS signals from the ocean with wind remote sensing application, *IEEE Trans. Geosci. Remote Sens.*, *38*(2), 951–964.